Dynamics of two microscale DPF devices

William Pollard Jr[1], Andrew Duggleby[2] and David Staack[1]

[1] Department of Mechanical Engineering, Texas A and M University, College Station, TX 77843, USA
[2] Exosent Engineering, LLC, 12600 Hwy 30, Suite 100, College Station, TX 77845, USA

E-mail: dstaack@tamu.edu

CrossMark

Abstract

Dense plasma focus (DPF) devices are coaxial transient discharge devices capable of generating plasma densities greater than 10^{16} cm^{-3} with ion temperatures in excess of 1 keV by compression resulting from strong magnetic fields created by high pulsed current. They are predominately used for high energy particle generation, but they are also convenient for investigating pinch dynamics due to their relatively fast repetition rates. These devices have been extensively studied at length scales on the order of cm, and this work helps to bridge understanding of larger low pressure pinches and more recent moderate energy density sources with novel applications like portable sources for high energy particles. In this research, the dynamics of two significantly smaller DPF devices operating in 50–190 torr He at $<$5 J/pulse with anode radii of 550 μm and 100 μm have been investigated using a 50 ns gated ICCD to image discharges throughout their lifetimes. Typical discharge stages of breakdown, rundown, pinch and expansion are observed for the microscale DPF. Images during the breakdown process are compared with respect to their symmetry, the velocity of their features, and their relative pinch intensities. Applicable scaling parameters are also compared to those of other DPF devices. In addition, the applicability of Knudsen scaling to DPF operation is introduced. The images show that as the anode radius decreases, breakdown and rundown features tend towards symmetry at higher pressure and near the Paschen minimum.

Keywords: dense plasma focus, plasma dynamics, microscale plasma, plasma imaging, Knudsen scaling

(Some figures may appear in colour only in the online journal)

1. Introduction

The dense plasma focus (DPF) is a coaxial plasma discharge device with a central anode, outer cathode electrodes and one open end. DPF devices are capable of generating regions of dense high temperature plasma by rapidly pulsing current between the anode and cathode in a low pressure environment. Current densities in DPF devices are sufficiently high that self-induced magnetic fields dominate the dynamics of the plasma. The magnetic fields can localize and confine the energy release to a region near the anode tip. While these effects are brief, usually lasting only nanoseconds, plasma densities can be greater than 10^{19} cm^{-3}, and ion temperatures on the order of 1 keV can be achieved [1–4].

Because they are so effective at creating highly energetic compressions, DPF devices are used as sources of x-rays and neutrons as well as generators for ion and electron beams [4].

DPF devices have been tested across a wide range of energies and sizes from the larger devices, $\sim$10 cm in diameter, which may consume energy on the order of MJ, to the smaller devices, $<$1 mm in diameter, which operate at less than 1 J. The most well studied DPFs are those in the United Nations University/International Centre for Theoretical Physics Plasma Fusion Facility(UNU/ICTP PFF) network. These DPF devices were constructed by the Asian-African Association for Plasma Training. The UNU/ICTP PFF network consists of at least six similar DPF devices all of which operate on the order of 1 kJ [5]. Given the wide array of capabilities, it is not surprising that DPF devices have found an equally wide array of practical and theoretical applications. Such applications are materials processing [6–13], neutron generation (creation of radioisotopes, neutron imaging, equipment calibration, fast neutron activation analysis) [14–20], x-ray generation (radiography, microlithography) [21–26], fusion research [27–30],

object detection (active interrogation) [31, 32], and even medical applications [33].

DPF devices generally come in two geometric variations based on the aspect ratio of the anode length to its diameter, ℓ/D. Mather-type configurations have anodes that are longer than they are wide such that $\ell/D > 1$ where a ratio in the range of 5–10 is typical. The other type of configuration is the Filipov type where $\ell/D < 1$ [3]. There are several ways in which the cathode may be situated around the anode. For one, the anode and cathode may be configured as coaxial cylinders with a dielectric interface between the two at one end. In a slight modification to the coaxial arrangement, a squirrel cage setup is one in which the anode is surrounded by a set of evenly spaced cathode pins equidistant from the anode axis. In yet another arrangement, the anode is insulated by a dielectric and left to protrude from a conductive surface that is cathode. This last anode/cathode arrangement was used in our experiments. The last two configurations have open cathodes which allow for radial expansion and prevent plasma flow stagnation at the cathode surface and thus improve the quality of the device [2].

The operation of a DPF device can be divided into three distinct phases. The first phase is the initial breakdown. During this stage, the voltage applied to the central anode reaches the breakdown voltage which is controlled by environmental and geometric conditions as well as insulator properties. The second phase is the rundown phase during which the current sheath is accelerated by $\mathbf{j} \times \mathbf{B}$ forces to the end of the anode, and a parabolic current sheath develops. The current sheath is both a propagating ionization wavefront and the motion of ionized gas moving in the direction of the anode tip and is different from a plasma sheath which is more similar to a fluidic boundary layer. The vertex of the parabolic current sheath is located at the exposed tip of the anode, expanding in the direction of the cathode, and ideally the sheath development is azimuthally symmetric. Finally, in the pinch phase these same $\mathbf{j} \times \mathbf{B}$ forces acting around the central electrode tip cause a concentration and confinement of the plasma to the tip of the anode. Elevated temperatures and plasma densities occur during the pinch phase and are maximized when the circuit is timed to peak current as the sheath reaches the anode tip, collecting and pushing gas into this region by the $\mathbf{j} \times \mathbf{B}$ forces in the so called snowplow effect. A significant portion of the confined plasma may escape along the axis, and very intense pinches do not always occur given this geometry. Other deficiencies are asymmetric breakdown phases resulting in $\mathbf{j} \times \mathbf{B}$ forces not leading to compression at the tip [2], or poor timing of current peaking during the end of the rundown phase [3].

DPF devices of various sizes tend to share similar derived parameters, and they are useful as guidelines in the design of DPF devices. The PF-1000, one of the largest DPF devices, operates above 1 MJ and has an anode radius of 6.1 cm whereas the PF-50 J is by comparison one of the smaller devices, operating with 50 J and a 0.15 cm anode radius [34]. The radius of the anode, a, can be used to predict the size of the pinch which is assumed to be cylindrical having a radius of $\sim 0.12a$, length of $\sim 0.8a$ and a volume of $V_p = 0.036a^3$. Even though the operating energies, E, of these devices can differ by 4 orders
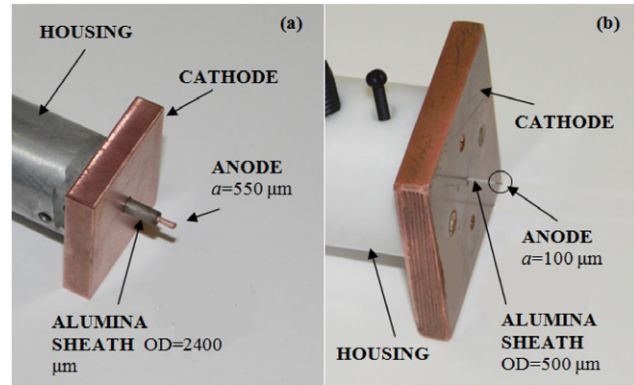

Figure 1. DPF anode cathode assemblies. (a) $a = 550$ μm, (b) $a = 100$ μm. These are among the smallest DPF anodes tested to date.

of magnitude, their energy density (*ED*) parameters, given by $ED = 28Ea^{-3}$, differ by less than one order of magnitude. In optimized devices the energy density parameter is on the order of 10^{10} J m^{-3}. Another important scaling quantity is the drive parameter (*DP*), which is given by $DP = I_0 p^{-0.5} a^{-1}$, where I_0 is the peak current and p is the environmental filling gas pressure. The drive parameter is typically in the range of 65–95 kA mbar$^{-0.5}$ cm^{-1} for all optimized DPF devices, and it controls the radial and axial plasma velocities. Devices of similar drive parameters, have comparable characteristic velocities and temperatures [35]. Furthermore, during the rundown and pinch phases both the current sheath's radial and axial velocities, v_r and v_a respectively, are proportional to the drive parameter and in the range of ~ 1–2.5×10^5 m s^{-1}. The microscale DPFs investigated in this research have characteristic velocities of ~ 1–4×10^4 m s^{-1}.

Since focus devices are effective in generating high energy particles, scaling laws for neutron and x-ray production are of practical importance. Experimental and numerical results of neutron yield, Y, in deuterium seem to follow scaling that suggests $Y \sim I_{\text{pinch}}^{3.3-4.5}$ [34, 36]. X-ray emission is highly gas dependent and has been found to scale as $E_{\text{xray}} \sim I_{\text{peak}}^{3.2-5.5}$ [3, 36]. Considerable numerical analysis for neutron and x-ray scaling has been conducted by Lee and is evident in the success of his 5 phase model, which shows good agreement with experiments involving low inductance Mather type focus devices with $E > 1$ kJ [37, 38].

A motivation for building lower energy devices—those with small anode radii—is so that rapidly firing radiation sources may be investigated. Rapid firing radiation sources tend to be smaller and are thus more portable. Furthermore, since they are rapid firing devices, they can maintain sufficient flux of high energy particles. Such devices may be amenable for fieldwork involving substance detection [15, 39].

Researchers led by Soto have pioneered the miniaturization of the DPF device. They have shown evidence of pinch in the PF-50 J ($E = 50$ J, $a = 6$ mm) and also in the nanofocus (NF) device ($E = 0.1$ J; $a = 0.8$ mm) using optical techniques and voltage/current waveform analyses [40–42]. Using a proportional ^{3}He counter, they were able to show neutron emissions on the order of 10^4 neutrons per shot in the PF-50 J device.
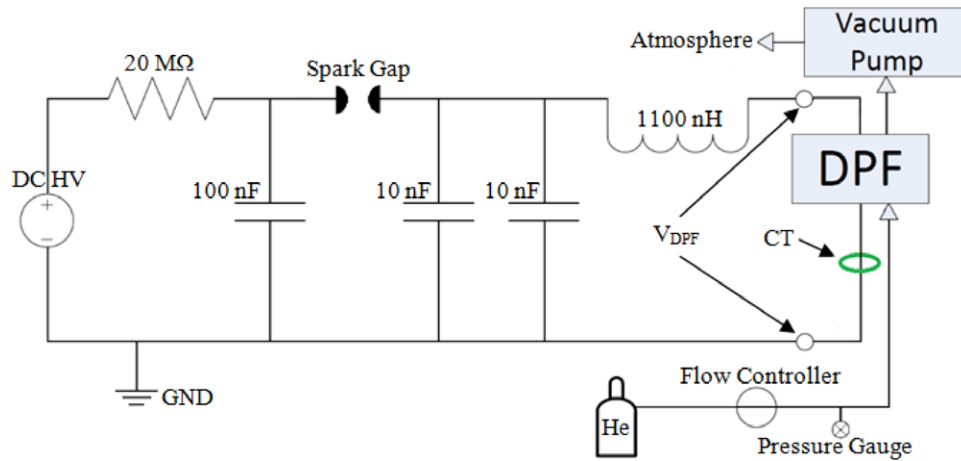
Figure 2. Annotated schematic of experimental setup showing pulsing circuit, gas regulation, and electrical measurements.
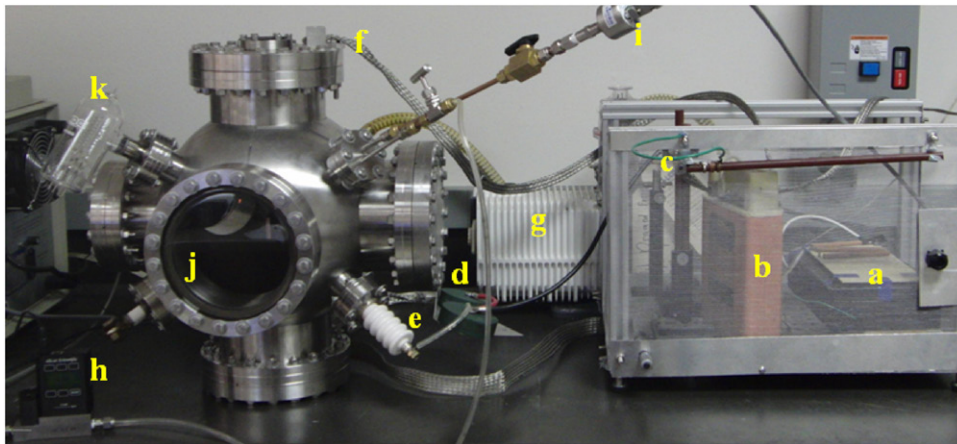

Figure 3. DPF experimental setup. Power supply not pictured. Annotated components are as follows: (a) 20 MΩ ballast resistor, (b) 100 nF primary capacitor, (c) variable spark gap (occluded), (d) two 10 nF secondary capacitors wired in parallel, (e) high voltage feedthru, (f) ground connection (current transducer not shown), (g) vacuum pump, (h) gas flow controller, (i) pressure gauge, (j) optical port. *Note: the ionization pressure gauge (k) was not used in the experiment.*

In their work on the PF-50 J, Moreno *et al* captured highly time resolved images of the rundown phase, the pinch, and even the lifting of the pinch off of the anode [41]. They note how the evolution of the current sheath is the same in this device as it is in those that operate at energies several orders of magnitude higher. However, in their work on the very smallest DPF, the nanofocus ($a = 200$ μm) device [40], a full description of the current sheath's evolution is absent. Energy density and drive parameters for the nanofocus have been calculated as 3×10^{11} J m^{-3} and 126 kA mbar$^{-0.5}$ cm^{-1}, respectively.

In this paper, temporally resolved dynamics of two small protruding Mather-type microscale DPF devices are explored. Previous work with microscale devices has done an excellent job demonstrating and characterizing miniaturized DPF operation, but little attempt has been made to capture and describe the entire lifetime of microscale pinch phenomena in terms of their characteristic features. This work serves to fill in these gaps with the hopes that it will lead to a better understanding of the pinching process which will result in more reliable operation of smaller devices. Advantages of miniaturizing these devices are explained shortly. This work also helps to bridge
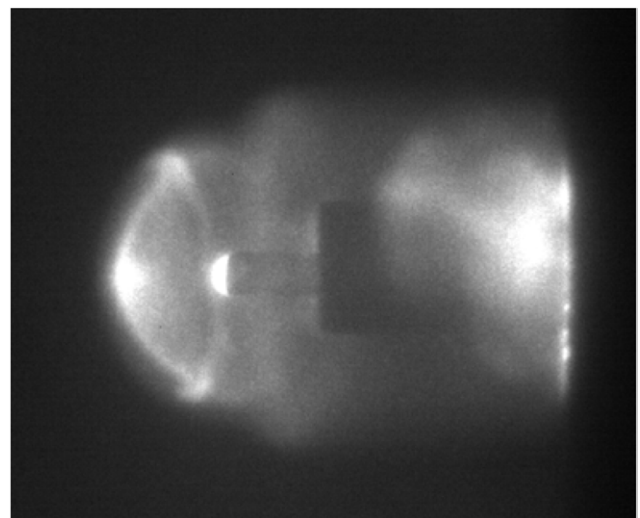

Figure 4. DPF ($a = 550$ μm) firing in 130 torr He at 17 kV. This image was collected using a 700 ns trigger delay and a 50 ns integration time. Subsequent voltage and current traces were collected from this individual firing.

understanding of larger low pressure pinches and more recent moderate energy density sources with novel applications like portable sources for high energy particles. A secondary contribution of this work is to further validate DPF operation at micrometer length scales. The larger of the two operates with $a = 550$ μm and stored energy of $E \sim 2$ J. The second device operated with similar energy but had anode radius of $a = 100$ μm. Miniaturized DPF devices are of interest because efficiency of high energy neutron production may scale as a^{-3} assuming Knudsen and DPF scaling parameters are maintained. As a decreases, operation at increased pressure is required to maintain scaling, and since maintaining symmetry is an important factor in ensuring effective pinching, close examination of breakdown and rundown phases is necessary. This research proposes that Paschen scaling following pa may also need to be maintained for pinching. Plasma dynamics were visualized using the plasma visible luminescence and a nanosecond gated ICCD camera. Sequential 50 ns exposures at 100 ns intervals spanning 1 μs were captured from the onset of breakdown through the post pinch expansion. Images were collected and compared for a test matrix of three pressures and three operating voltages. Breakdown asymmetries, rundown features and luminous intensities were evaluated from the images and scaling parameters were also compared to those in the literature. Both devices are among the smallest DPFs tested. Their small size makes convenient the analysis of pinch dynamics using several thousand repetitious firings. Both devices were operated in helium, and neither neutron nor x-rays were sought. Observed microscale dynamics indicate promise for applications to rapid firing neutron sources organized in microscale arrays. Optimization of the current setup is still required.

2. Experimental setup

Two protruding type anode cathode assemblies were used in this experiment, and they are shown in figure 1. The larger of the two assemblies shown in figure 1(a) had a copper wire anode with $a = 550$ μm insulated by an alumina sleeve having $OD = 2400$ μm and a 5 mm square copper block cathode. The alumina insulator extended 7 mm beyond the cathode backplane, and the anode extended 3 mm beyond the alumina. The anode of the smaller assembly shown in figure 1(b) was a tungsten wire of $a = 100$ μm radius insulated by an alumina tube with $OD = 500$ μm. A copper block was again used for the cathode. The insulator in the smaller system protruded 4.5 mm from the cathode, and the tungsten anode extended 2.3 mm beyond the alumina. The electrode housing shown behind the cathode contains electrical connections, and it was designed so that the insulator protrusion length was adjustable. Set screws were used to secure the alumina insulator. Electrode assemblies were mounted in and electrically grounded to a vacuum chamber backfilled with helium at flow rates such that chamber pressures were in the range of 50–190 torr. Industrial grade helium flowed continuously through the vacuum chamber to maintain purity.

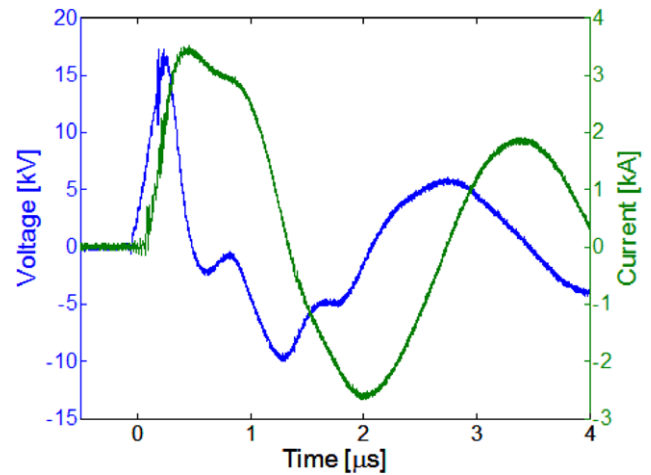To power the DPF, a high voltage dc power supply was connected through a 20 MΩ ballast resistor to a variable

Figure 5. Voltage and current characteristics of DPF ($a = 550$ μm) firing in 130 torr He. Voltage and current rise times are 300 and 350 ns, respectively.
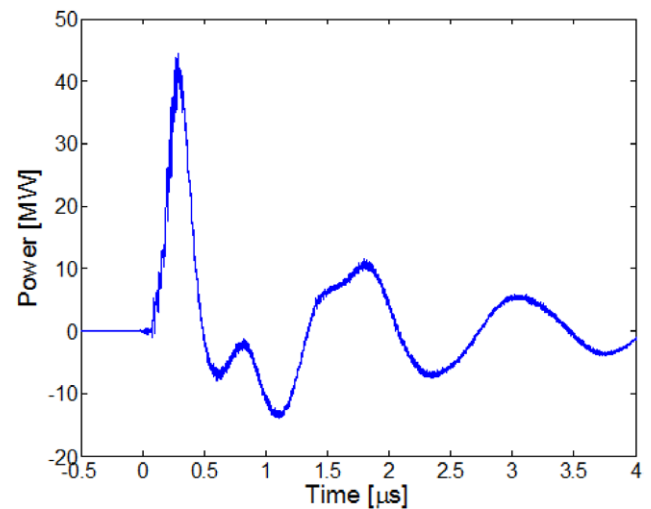

Figure 6. Power delivered during pinch process corresponding to voltage and current waveforms shown in figure 5. Peak power is delivered around 300 ns, which is approximately the end of the rundown phase.

length spark gap in parallel with a 100 nF primary capacitor. The variable length spark gap controlled voltage across the primary capacitor. Down-current of the spark gap, two 10 nF low inductance secondary capacitors were connected in parallel, providing 20 nF of equivalent capacitance, and the secondary capacitors were connected in parallel with the DPF electrode housing. The DPF connects to ground through the vacuum chamber. Self-inductance in the circuit down-current of the spark gap was measured using an LC meter as 1100 nH, which is high in comparison to other DPFs where inductance is typically on the order of 10–100 nH [3]. The DPF device was fired at a rate of 0.5 Hz, limited by the RC circuit and the current supplied by the dc power supply. A schematic of the experimental setup is shown in figure 2 and an annotated image is shown in figure 3.

Images were collected using Stanford Computer Optics 4-picos ICCD camera through a glass optical port on the vacuum chamber. The light was filtered by the vacuum

Table 1. Test condition matrix for the $a = 550\ \mu$m DPF.

Condition	1	2	3	4	5	6	7	8	9
P_{He} [torr]	50	50	50	125	125	125	190	190	190
V_{DPF} [kV]	10	14	19	10	14	19	10	14	19
I_{DPF} [kA]	2.3	2.3	2.3	2.9	2.9	3.2	3.7	3.8	3.8

chamber window and camera spectral response. The camera responds to light in the 200–900 nm band, but the window is glass and removes some of the ultraviolet. The acquired light is roughly in the 300–900 nm spectrum. EMI from breakdown in the spark gap was detected by a 5 cm antenna and used to trigger image acquisition in order to avoid cable delays. Internal gating delays are inherent in the ICCD and are specified by the manufacturer as 75 ns.

DPF voltage and current were measured as indicated by figure 2 on a DPF anode/cathode assembly similar to those shown in figure 1(a). The anode/cathode assemblies used while measuring voltage and current had a shorter anode insulator protrusion length. Changing the protrusion length alters the rundown time which is important for peak power timing. Therefore, the electrical signals presented are similar to those of the anode/cathode assembly used during optical analysis. Voltage and current signals were acquired via a LeCroy 204MXi Waverunner oscilloscope triggered by voltage rise. Voltage was measured using a North Star PVM-4 40 kV voltage probe, and current was measured using a Pearson M#101 current transducer (CT). A 50 ns time integrated image is shown in figure 4 of the anode/cathode assembly used for electrical diagnostics 700 ns after spark gap firing. Similar visible features are apparent upon comparison of the image in figure 4 to those used for dynamic analysis to be presented in the following section. Voltage and current signals of the DPF pictured in figure 4 are provided in figure 5. Presented traces are believed to be representative of DPF operation regimes examined in these experiments. Waveforms in figure 5 show a peak voltage of 17.3 kV with rise time ~300 ns and peak current of 3.5 kA with a rise time ~350 ns and FWHM ~1 μs. Circuit ringing was observed in both signals and dissipated after 15 μs. Power delivered during the pinch process was calculated from voltage and current signals and is shown in figure 6. As will be shown in later figures, peak power is delivered after 300 ns, which is approximately the end of the rundown phase.

For the 550 μm anode, two sets of images were taken for each of nine test conditions which are described in table 1 with respect to gas fill pressure and peak voltage. The first set of images from the 550 μm anode configuration was taken with relatively high gain so that features were visible throughout the breakdown, rundown, pinch, and post pinch phases. Gain was held constant throughout a test condition but was adjusted between conditions to enhance visible features. Adjusting gain allowed for improved visualization of pinch dynamics but hindered luminous intensity assessment since pixel intensities were often saturated.

The second set of images from the 550 μm configuration was taken with a gain such that no images were saturated,

Table 2. Test condition matrix for the $a = 100\ \mu$m DPF.

Condition	b	c	d	e
P_{He} [torr]	85	85	150	150
V_{DPF} [kV]	4.7	9.4	4.7	9.4
I_{DPF} [kA]	0.7	0.9	1.8	1.8

and this level was held constant for all test combinations in this set. The purpose of this image set was to detect local regions of relative intense brightness and to allow for cross condition peak intensity comparisons. All images in both sets were taken with an integration time of 50 ns, and collected in delay increments of 100 ns from 0 to 1000 ns providing 11 images for each experimental condition. Intensely bright regions correspond to high energy and high plasma density. Regions of intense brightness at the anode tip are indicative of a pinch event, and in some cases evidence of a pinch can only be observed optically because electrical signals do not show the characteristic dip in the dI/dt trace accompanied by a simultaneous voltage spike [43, 44].

For the $a = 100\ \mu$m DPF only one set of saturated images was captured, and the test matrix for these experiments is given in table 2. Images were taken at combinations of two pressures and two DPF voltages. Using an image integration time of 100 ns and a delay between images of 100 ns 11 images were captured between 0 and 1000 ns, similar to the case of the 550 μm anode DPF. ICCD gain was set sufficiently high such that features were visible throughout the pinch process. An unsaturated comparison was not made for the smaller DPF.

3. Results

Figure 7 shows two typical images of a discharge. The image in figure 7(a) shows the 550 μm DPF during the rundown phase, and the image in figure 7(b) shows how the plasma develops after the pinch occurs. These images were taken with high gain and portions of the images are saturated as is indicated by the regions of bright white color. Geometries of the devices visible in these images are the anode, the alumina dielectric, and the cathode plane. Also apparent are several characteristic features of the plasma, more clearly understood from later results but introduced here. First is the current sheath, which surrounds the alumina and runs down towards the anode tip. The pinch occurs when the sheath reaches the
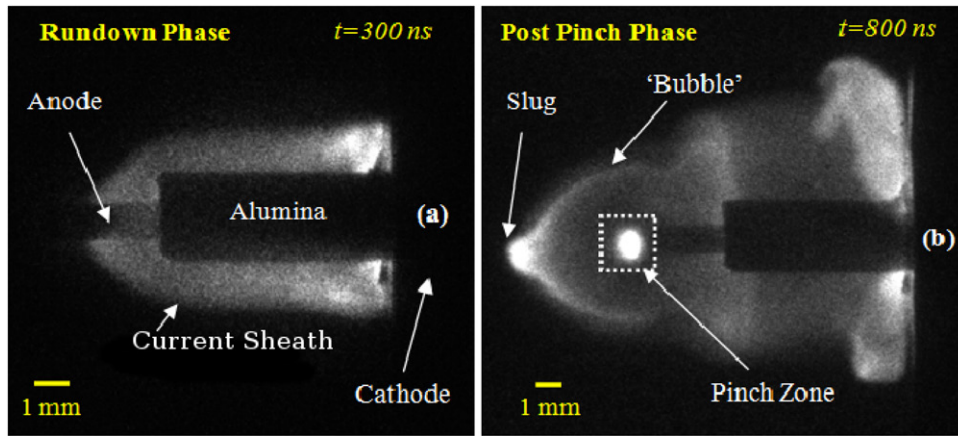
Figure 7. Annotated images of pinch process showing characteristic features in the $a = 550\ \mu$m DPF used for optical diagnostics in pinch dynamic analysis. (a) Rundown phase, (b) Post-pinch phase.
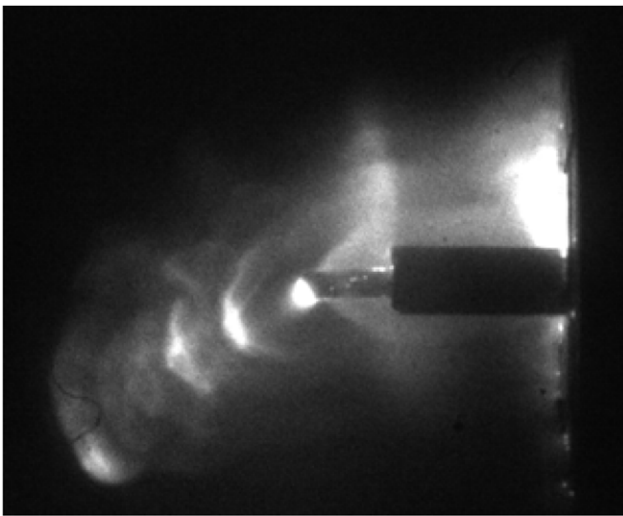

Figure 8. Multi-exposed image of a single firing of the 550 μm DPF. Individual images have exposure times of 50 ns, and the delay between images is 300 ns.

anode tip at approximately 300 ns, and an intensely bright region is present at the anode tip during the time of the pinch. Peak power is delivered around this time as shown in figure 6. Second are radially expanding spherical (at the tip), and cylindrical (along length of anode and dielectric) shock fronts of the higher temperature plasma region expanding into the cool background. The expanding spherical shock front is termed the 'bubble'. Third is an apparent slug of plasma which has been ejected from the pinch region. Lastly, a build-up of plasma is observed flowing against the cathode wall.

A multi-exposed image of a single pinch event under condition 5 as described in table 1 is shown in figure 8. Individual images each have an exposure time of 50 ns, and using a delay of 300 ns between images, several images from a single pinch event were captured and then combined with one another. This image is representative of how the pinch evolves in a single firing. A false color set of the saturated images showing the dynamics of the pinch evolution under all nine conditions for the 550 μm DPF is provided in figure 9. Each image in figure 9 was taken from separate firings of the

DPF. As such, the images are qualitative representations of one pinch. By examining plasma slug locations in figure 9 it is clear that each image is from separate firings. For example, at $t = 1000$ ns in condition 3, the slug is shown moving towards the bottom right of the image, whereas at the previous time the slug is observed moving to the top right. Regions that are pink in color indicate brightness saturation. An unsaturated set of images for condition 5, indicated as 5′, is included in figure 9 for comparison of relative brightness intensities. The condition 5 images show the pinch, which is circled by a dotted yellow line, as being far more luminous than any other area in the field of view. In fact, the anode tip is approximately 30× brighter than any other area in the field of view as is demonstrated in figure 10. This is determined by comparing relative intensities after subtracting background from the signal. Therefore, the energy density at the anode tip is much greater than any surrounding area. The range of drive factors for conditions 1–3, 4–6 and 7–9 are 5–8, 3–5 and 3–4 kA mbar$^{-0.5}$ cm^{-1}, respectively, which are <10% of the typical range of 65–95 kA mbar$^{-0.5}$ cm^{-1}, setting an expectation for radial and axial sheath velocities less than those of optimized devices.

Timing of the image sequence begins at breakdown in the spark gap and is initiated by detection of EMI through an antenna. After the discharge in the spark gap, initial breakdown occurs between the DPF anode and the cathode, and a thin current sheath forms around the alumina. The sheath accelerates towards the anode tip, expanding radially, and the pinch occurs when the sheath reaches the anode tip and $\mathbf{j} \times \mathbf{B}$ forces compress the plasma to high temperature and pressure. Initial concerns of whether or not the bright spot indicated a pinch were quelled by the observation that the presence of a bright spot at the anode tip was sensitive to gas pressure for the same applied voltage, so pinching and non-pinching conditions were easily discernible at similar input energy. If the anode spot was due to heating it should be present in all conditions with similar input energies. In these image sequences the pinch is observed after 300 ns in all cases. Subsequent images show how the plasma returns to quiescence after the pinch. These images indicate that pressure has a more pronounced effect on breakdown/rundown symmetry than does energy input. For relatively large diameter coaxial electrode
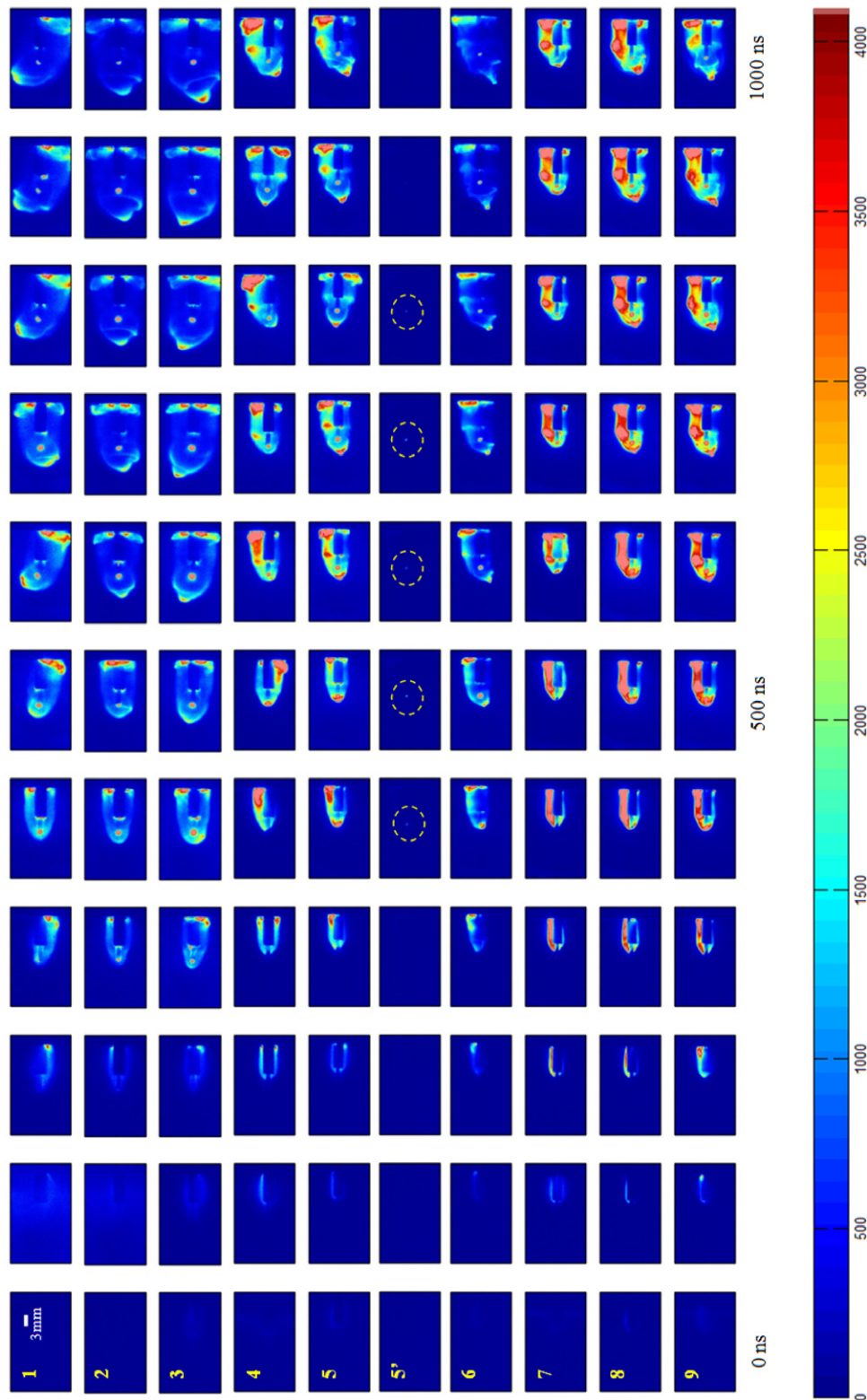
Figure 9. Saturated ICCD images of the 550 μm DPF. Saturated areas are shown in pink. All test conditions are shown. Image sequence 5′ shows the corresponding unsaturated ICCD images. The unsaturated pinch area is indicated by the broken circle.

arrangements, gas pressures >15 mbar can result in discharges between the electrodes that disrupt pinching [45] and tend towards asymmetry as Knudsen scaling moves away from the Paschen minimum, and in fact, most prior research on DPF devices has been confined to operating pressures in the 1 mbar range. Typical *pa* values for cm scale DPF are in the 1–10 torr-cm range [3], which is similar to the range of *pa* explored in this work.

3.1. 550 μm DPF

Two distinct trends are evident in the saturated images of the 550 μm anode DPF shown in figure 9. The first is that as pressure increases, the current sheath becomes more confined to the anode axis and tends towards asymmetry. Lower pressure conditions show the current sheath appearing diffuse, and as pressure increases the breakdown is more closely confined to a preferred side of the dielectric/gas interface region. Higher pressure conditions show breakdown occurring most strongly in the region above the anode. This could be a result of imperfect anode geometry. Small deviations from a perfect coaxial arrangement can encourage bias in the breakdown direction due to stronger electric fields. The second trend evident is that at increased energy input (higher voltage) the presence of the slug feature becomes more pronounced. At $t = 600$ ns in all high voltage conditions (3, 6 and 9), the slug is prominent even though it is smaller in size as compared to its lower energy counterparts. The slug is most likely composed of gas being squeezed out in the axial direction during the compression process. The slug departure angle can be as much as 70° off the axis, but since the images are from individual firings, it is not clear whether or not the slugs trajectory is influenced by **B**-fields.

Dynamics of the features described in figure 7 are plotted alongside the unsaturated peak intensity of the brightness in figure 11. Since these images are captured at a common gain, luminous features of relatively weaker pinches are undetectable, but this is necessary for consistent comparison. During the initial rundown phase, peak intensity maintains low levels in all conditions. Generally, peak intensity increases as the current sheath travels toward the anode tip, reaching its maximum as the sheath approaches the anode tip. In low voltage conditions 1, 4, and 7 there is little variation in luminous intensity throughout the pinch, and furthermore, in these same conditions there are no sudden changes in luminous intensity. This is most likely due to filtering caused by ICCD gain selection since DPF features are similar across all conditions indicating similar behaviour. For most all other conditions the rise time of luminous intensity is about 200 ns. That the rapid increase in luminous intensity occurs simultaneously with the sheaths arrival at the anode tip likely indicates the occurrence of a pinch as previous research has demonstrated [43, 44]. From event to event luminous intensity appears to vary by 25% due to initial asymmetry or shot to shot variation. As this is an unoptimized DPF, the pinching occurs over longer time scales than those typically reported for small-scale DPF devices [40] due to slower peak current rise times which are due to higher inductance in the external pulsing circuit. The energy densities for the 10, 13 and 19 kV conditions are 2, 3 and 6×10^{11} J m^{-3}, and this is reflected in figure 11 by row-wise comparison of luminous intensity.

The sheath, bubble and slug velocities are indirectly shown in figure 11 as the slopes of the position profiles. Sheath velocity has a maximum of $\sim$40 000 m s^{-1} under condition 3 (19 kV/50 torr) and minimum of $\sim$8000 m s^{-1} under condition 7 (10 kV/190 torr). Because drive parameters are roughly 10% of the lower limit of the idealized

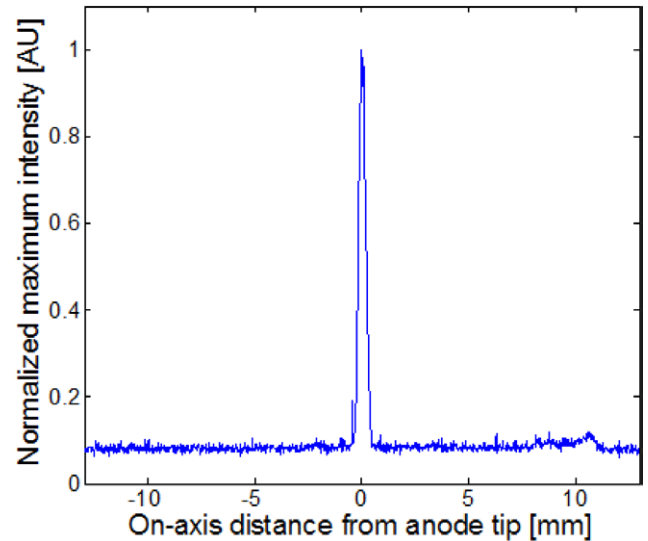**Figure 10.** Normalized column-wise maximum brightness intensity for unsaturated condition 5′ at $t = 500$ ns. The pinch at the anode tip is 30× brighter than surrounding areas. The cathode is located at +11 mm.

range of 65–95 kA mbar$^{-0.5}$ cm^{-1}, reduced sheath velocities are expected, especially at increased pressure. Generally, the sheath velocity is greater than both the bubble and slug velocity with this effect being most pronounced in condition 3. Average sheath velocity decreases as pressure increases and increases as input energy increases.

Average velocity data for the features is summarized in table 3. Slug velocities show similar response to pressure and input energy and is observed to range between 5000–15 000 m s^{-1}. The slug velocity is proportional to the input energy and inversely proportional to pressure. Both of these observations are consistent with drive parameter scaling. Slug velocities are determined assuming straight-line displacement from the anode tip, and as such they are a minimum value as any curvature in the trajectory is neglected. No correlation is observed with input energy and average bubble velocity, which ranged from 4500–9500 m s^{-1}, but bubble velocity decreases with increasing pressure as the higher density retards plasma expansion.

Bubble expansion could be due to either thermal expansion (neutral sound speed) or ambipolar diffusion (ion sound speed). Since no data were collected for either electron or ion temperatures, it is not possible to say that this is an equilibrium plasma, and therefore the driving factor of the bubble's velocity remains unclear. The bubble expands with some characteristic velocity, and from that a characteristic temperature of either emitting neutrals or electrons can be estimated. The characteristic temperature can be estimated using the relation $V_{rms} = \sqrt{\frac{3k_BT}{m_{ion}}}$, where V_{rms} is the measured characteristic root mean square speed, k_B is the Boltzmann constant, T is the characteristic temperature and m_{ion} is the mass of a helium ion. Characteristic temperatures for the 50, 125, and 190 torr conditions are thus in the range of 0.28–1.25 eV. At higher pressures there is less energy per unit mass resulting in lower characteristic temperatures. If expansion is thermally driven,
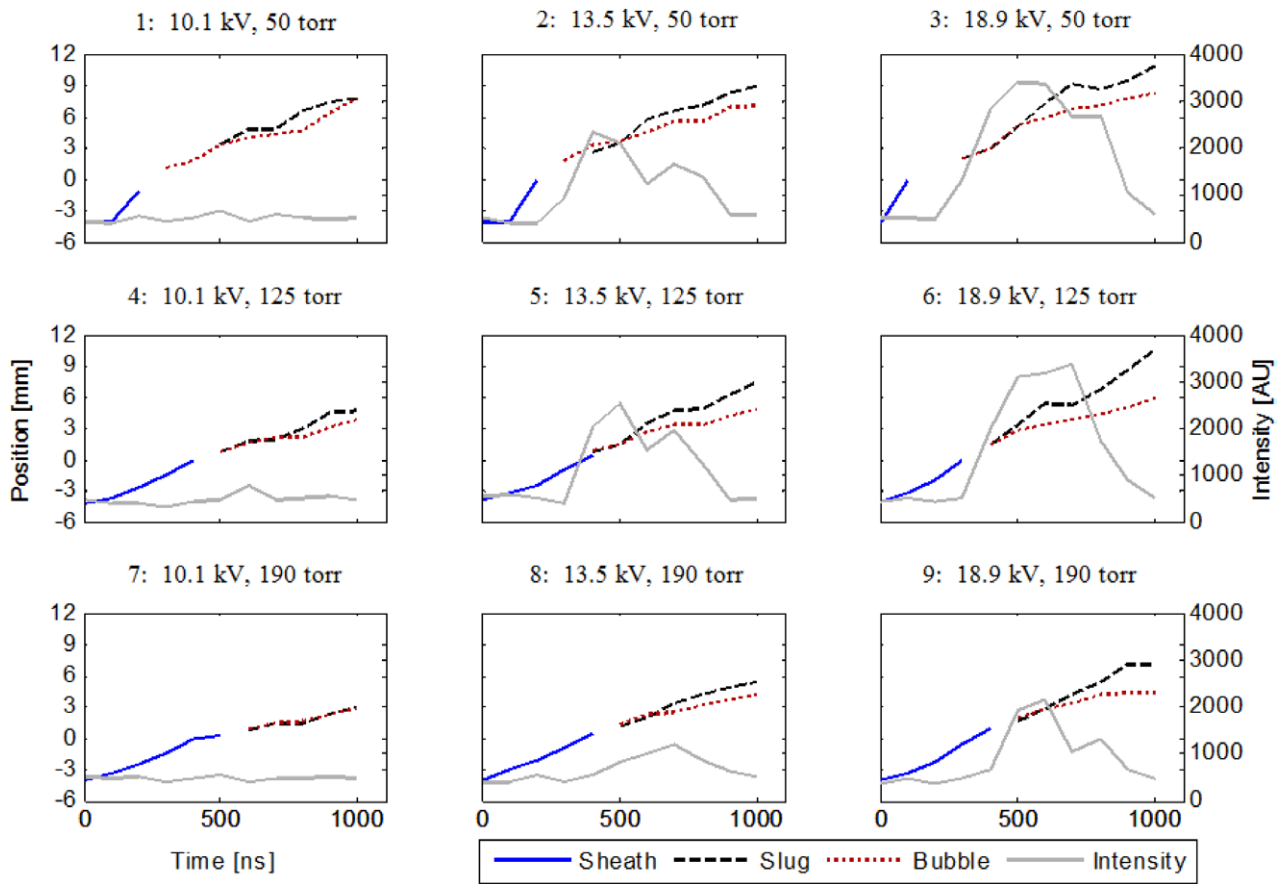
Figure 11. Spatial evolution of plasma in 550 μm DPF device plotted with peak brightness intensity from unsaturated images. Positions are relative to the anode tip. Experimental conditions are provided above individual plots.

Table 3. Summarized average velocity data for features observed in the $a = 550$ μm DPF.

Condtion	Pressure [torr]	Voltage [kV]	Drive Param [kA mbar$^{-0.5}$ cm^{-1}]	Average Velocity [m s^{-1}]		
				Sheath	*Bubble*	*Slug*
1		10.1	5	14,920	9,423	8,992
2	50	13.5	6	20,375	7,680	10,586
3		18.9	8	41,470	9,143	12,703
4		10.1	3	10,187	5,931	7,624
5	125	13.5	4	10,985	6,647	11,036
6		18.9	5	13,153	7,378	15,299
7		10.1	2	8,439	4,741	5,285
8	190	13.5	3	11,068	5,726	8,794
9		18.9	4	12,271	4,764	10,907

then this is an ion temperature and representative of an equilibrium plasma. On the other hand, if the expansion is driven by ambipolar diffusion, then this is an electron temperature and represents a non-equilibrium plasma.

3.2. 100 μm DPF

Saturated images from the 100 μm anode DPF are shown in figure 12, and as was done for the images in figure 9, images

in figure 12 were taken from individual firings of the DPF and are therefore only representative of average behaviour. Again the ICCD was triggered by breakdown in the spark gap to minimized cable delays. The image sequences show sheath formation at breakdown between anode and cathode followed by sheath advance towards the anode tip where it undergoes radial expansion. The pinch appears to occur around 500 ns based on the position of the current sheath. Because the images are saturated, comparisons of light intensity during the process
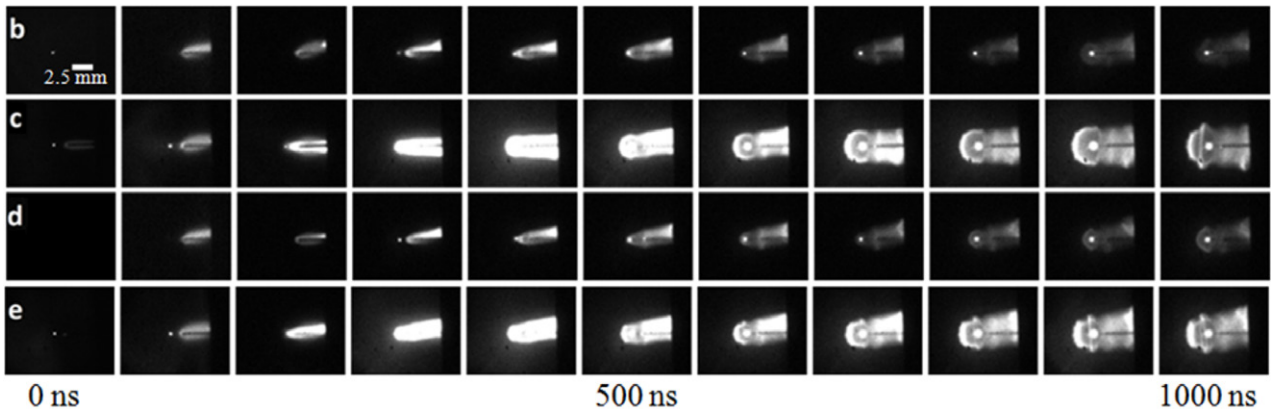
Figure 12. Saturated images of the 100 μm DPF. The test condition letter is given in $t = 100$ ns images.

Table 4. Summarized average velocity data for features observed in the $a = 100$ μm DPF.

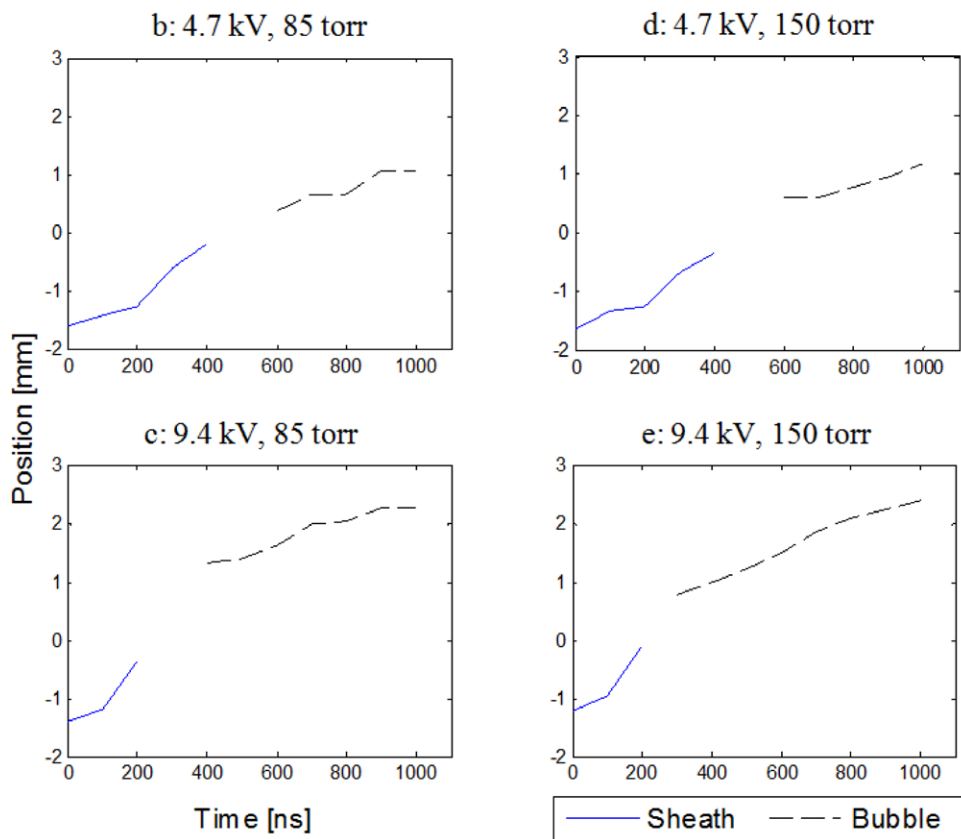| Condtion	Pressure [torr]	Voltage [kV]	Drive Param [kA mbar$^{-0.5}$ cm^{-1}]	Avg Vel [m s^{-1}] Sheath	Avg Vel [m s^{-1}] Bubble
b	85	4.7	6	3,514	1,695
c	85	9.4	17	5,160	1,605
d	150	4.7	5	3,225	1,488
e	150	9.4	13	5,504	2,310

Figure 13. Spatial evolution of plasma in 100 μm DPF device. Position is given relative to the anode tip. Experimental conditions are provided above individual plots.

are not possible. However, symmetry is assessed and velocities of characteristics described in figure 7 are examined. As compared to the images in figure 9, the images in figure 12 show spatially consistent sheath and bubble development with a high degree of axial symmetry. This is especially noticeable in conditions *c* and *e* where the process is nearly symmetric. It appears that Knudsen scaling should be applied to small DPFs to achieve reliable and symmetric breakdown/rundown, and this criteria has not been explored in prior work. At the Paschen minimum location of breakdown is more controlled and streamer formation, a process that would lead to asymmetry due to space charge, can be avoided. Energy density parameters of this device are 6.2×10^{12} and 2.5×10^{13} J m^{-3} for the 5 and 9 kV conditions, respectively, which are roughly 2–3 orders of magnitude greater than energy densities found in optimized devices of larger diameter. The bright region at the anode tip is larger than the anode diameter, and the actual energy density may be lower than that determined by calculation based on electrode geometry alone. The figure 12 images show that the pinch radius is about 5× larger than the anode radius which would make the energy density comparable to optimized devices.

Several qualitative observations can be made from the images in figure 12. The first observation is the absence of a slug in all conditions. Second, axial symmetry is improved with higher energy input. Third, bubble presence becomes more distinct and appears at earlier times at higher energy input. In conditions *c* and *e* the bubble is well defined at $t = 600$ ns, whereas the bubble is present, but not as distinct, at $t = 900$ ns for the *b* and *d* conditions. Fourth, a small point of intense light is noticeable in the pinch region at the anode tip. This bright point is also visible in the saturated images of the 550 μm DPF and hints at pinching. Lastly, the dynamics of the 100 μm DPF do not appear to respond to increased pressure. Comparison of conditions *b* to *d* and *c* to *e* do not reveal significant qualitative variation.

Average velocity data for the 100 μm DPF is summarized in table 4, and dynamics of the 100 μm DPF under the four conditions are plotted in figure 13. For the 100 μm DPF, pressure and energy input have very different effects on the sheath and bubble velocities as compared to the 550 μm DPF. The 100 μm DPF sheath velocity ranges between 3200 m s^{-1} for condition *d* and 5500 m s^{-1} for condition *e*, and the drive parameters are 5 and 13 kA mbar$^{-0.5}$ cm^{-1}, respectively. The drive parameters for conditions *b* and *c* are 6 and 17 kA mbar$^{-0.5}$ cm^{-1} and remain 10–25% of the idealized range, and the sheath velocities are 10% of optimized DPFs. Sheath velocity appears to be sensitive only to energy input at these pressures, whereas with the larger DPF sheath velocity was sensitive to both energy input and pressure. The bubble velocity of the 100 μm DPF ranges from 1600–2300 m s^{-1} and is only sensitive to energy input in the high pressure condition. Using the same analysis as described for the $a = 550$ μm anode, characteristic temperatures for the 100 μm DPF were in the range of 0.04–0.09 eV. Bubbles are visible in all conditions of the 100 μm DPF, but the most pronounced bubbles are seen in condition *c* and *e*. The bubbles become noticeable at $a = 500$ ns and eventually deform most likely to shock

interactions, and features observed here have been observed in prior work on larger devices [46].

4. Conclusions

Dynamics of two relatively high pressure <5 J Mather type microscale DPFs, one with an anode radius of 550 μm and the other with radius of 100 μm, have been compared both qualitatively and quantitatively by examining event symmetry, light intensity and velocity characteristics. Small sizes were investigated because such DPF systems may be portable, operate at high frequencies, and be capable of operating in parallel. Relatively high pressure was investigated to achieve Knudsen number scaling (in this context equivalent to Paschen scaling) similar to typical devices. Adjusting pressure (*pa* range from 1–3 torr-cm) can help maintain breakdown dynamics, initial symmetry, and final pinch symmetry. Though not optimized, typical rundown and pinch phases were experimentally observed at high pressure and small size. Generally, these results indicate that high pressure and small size should be further explored. Particularly considering, as introduced in this paper but not addressed experimentally, efficiency of neutron production may scale as a^{-3} when Knudsen and typical DPF (drive parameter and yield) scaling are maintained. Pressure may introduce collisional losses but can be optimized and addressed by faster timing and reduced inductances potentially achievable at small size.

As mentioned both devices showed characteristic DPF behavior. Regions of intense brightness at the anode tip coincident with peak power output indicate that the device is pinching, and the luminous intensity of the pinch was 30 times greater than that of the surrounding area. As expected pinch luminosity increases with drive parameter, but only when the breakdown is symmetric. Measured sheath velocities were negatively correlated with pressure and positively correlated with input energy, and bubble and slug velocities, while generally lower than the sheath velocity, were seen to decrease with increasing pressure. The DPF with 550 μm radius showed considerable spatial variation in both the rundown and pinch phases and appeared more symmetric at the middle pressure with breakdown being contracted at higher pressure, and initially diffuse breakdown and slug ejection off axis at lower pressures. The 100 μm device was notably more symmetric at these high pressures.

Compared to optimized DPF devices of larger diameter in lower pressure operation, gas pressures are two orders of magnitude higher, the DPFs in this study had energy densities as much as 100 times greater, and the drive parameter was a factor of 4–12 below that considered to the be standard range for pinching (65–95 kA mbar$^{-0.5}$ cm^{-1}) [3]. This likely resulted in the reduced observed sheath velocities. It should be noted that efficient pinching can occur outside this range of drive parameter [3, 40] and this range is not an absolute rule. Maintaining symmetry appears, in part, to be related to Knudsen scaling which is controlled by gas pressure and anode geometry, and an additional constraint of DPF operation may be that devices should strive to operate near but to the right of the Paschen minimum (*pa* range 1–3 torr-cm).

Acknowledgments

References

[1] Krishnan M 2012 *IEEE Trans. Plasma Sci.* **40** 3189
[2] Mather J 1971 *Plasma Physics. Part* B (*Methods in Experimental Physics* vol 9) ed R H Lovberg and H R Griem (New York: Academic Press) pp 187–249 (www.sciencedirect.com/science/article/pii/S0076695X08608625)
[3] Soto L 2005 *Plasma Phys. Control. Fusion* **47** A361
[4] Gribkov V 2007 *17th IAEA Technical Meeting on Research Using Small Fusion Devices (Lisbone)*
[5] Mulyodrono S, Smith A, Suryadif W U and Zakaullahf M 1988 *Am. J. Phys* **56** 1
[6] Chernyshova M, Ivanova-Stanik I, Karpiński L, Scholz M, Ulejczyk B, Demchenko I and Lee J 2006 *Czech. J. Phys.* **56** B237
[7] Hussain T, Ahmad R, Khan I, Siddiqui J, Khalid N, Bhatti A S and Naseem S 2009 *Nucl. Instrum. Methods Phys. Res.* B **267** 768
[8] Ghareshabani E, Rawat R, Verma R, Karamat S and Sobhanian S 2010 *Appl. Surf. Sci.* **256** 4977
[9] Zhang T *et al* 2007 *Plasma Sources Sci. Technol.* **16** 250
[10] Wang Z, Yousefi H, Nishino Y, Ito H and Masugata K 2008 *Phys. Lett.* A **372** 7179
[11] Rawat R, Lee P, White T, Ying L and Lee S 2001 *Surf. Coat. Technol.* **138** 159
[12] Khan I, Hassan M, Ahmad R, Murtaza G, Zakaullah M, Rawat R and Lee P 2008 *Int. J. Mod. Phys.* B **22** 3941
[13] Kant C R, Srivastava M and Rawat R 1997 *Phys. Lett.* A **226** 212
[14] McDaniel F D, Freeman B and Fowler C 1997 *5th Int. Conf. on Applications of Nuclear Techniques: Neutrons in Research and Industry* (Bellingham, WA: International Society for Optics and Photonics) pp 517–20
[15] Soto L, Silva P, Moreno J, Zambra M, Kies W, Mayer R E, Clausse A, Altamirano L, Pavez C and Huerta L 2008 *J. Phys. D: Appl. Phys.* **41** 205215
[16] Bernard A, Cloth P, Conrads H, Coudeville A, Gourlan G, Jolas A, Maisonnier C and Rager J 1977 *Nucl. Instrum. Methods* **145** 191
[17] Verma R, Rawat R, Lee P, Lee S, Springham S, Tan T and Krishnan M 2009 *Phys. Lett.* A **373** 2568
[18] Silva P, Moreno J, Soto L, Birstein L, Mayer R E and Kies W 2003 *Appl. Phys. Lett.* **83** 3269
[19] Yokoyama M, Kitagawa Y and Yamada Y 1989 *Dense Z-Pinches* vol **195** (New York: AIP) pp 530–4
[20] Asai H and Ueno I 1989 *Fusion Eng. Des.* **7** 335
[21] Bhuyan H, Mohanty S, Neog N, Bujarbarua S and Rout R 2004 *J. Appl. Phys.* **95** 2975
[22] Pavez C and Soto L 2010 *IEEE Trans. Plasma Sci.* **38** 1132
[23] Zambra M, Silva P, Pavez C, Pasten D, Moreno J and Soto L 2009 *Plasma Phys. Control. Fusion* **51** 125003
[24] Barbaglia M, Bruzzone H, Acuna H, Soto L and Clausse A 2009 *Plasma Phys. Control. Fusion* **51** 045001
[25] Verma R, Rawat R, Lee P, Krishnan M, Springham S V and Tan T 2010 *IEEE Trans. Plasma Sci.* **38** 652
[26] Hussain S and Zakaullah M 2007 *Mod. Phys. Lett.* B **21** 1643
[27] Conrads H 1990 *Nucl. Sci. Eng.* **106** 299
[28] Soto L, Pavez C, Tarifeño A, Cárdenas M and Moreno J 2008 *Proc. of the 22nd IAEA Fusion Energy Conf. (Geneva, 13–18 October 2008)*
[29] Saw S H and Lee S 2011 *Int. J. Energy Res.* **35** 81
[30] Soto L, Pavez C, Tarifeño A, Moreno J and Cárdenas M 2009 *Proc. of the 7th Int. Conf. on Dense Z-Pinches* vol **1088** (New York: AIP) pp 223–6
[31] Gribkov V, Dubrovsky A, Karpiński L, Miklaszewski R, Paduch M, Scholz M, Strzyzewski P and Tomaszewski K 2006 *Plasma and Fusion Science: 16th IAEA Technical Meeting on Research using Small Fusion Devices; XI Latin American Workshop on Plasma Physics* vol **875** (New York: AIP) pp 415–8
[32] Gribkov V, Latyshev S, Miklaszewski R, Chernyshova M, Drozdowicz K, Wi U, Tomaszewski K and Lemeshko B 2010 *Phys. Scr.* **81** 035502
[33] Paduch M, Miklaszewski R, Pimenov V N, Ivanov L I, Dyomina E V, Maslyaev S A and Orlova M A 2006 *Nukleonika* **51** 55
[34] Soto L, Pavez C, Tarifeno A, Moreno J and Veloso F 2010 *Plasma Sources Sci. Technol.* **19** 055017
[35] Lee P and Serban A 1996 *IEEE Trans. Plasma Sci.* **24** 1101
[36] Saw S *et al* 2010 *Energy Power Eng.* **2** 65
[37] Lee S 2014 *J. Fusion Energy* **33** 319
[38] Abdou A, Ismail M I, Mohamed A E, Lee S, Saw S and Verma R 2012 *IEEE Trans. Plasma Sci.* **40** 2741
[39] Soto L, Pavéz C, Moreno J, Pedreros J and Altamirano L 2014 Non-radioactive source for field applications based in a plasma focus of 2j: pinch evidence *J. Phys.: Conf. Ser.* **511** 012032
[40] Soto L, Pavez C, Moreno J, Barbaglia M and Clausse A 2009 *Plasma Sources Sci. Technol.* **18** 015007
[41] Moreno J, Silva P and Soto L 2003 *Plasma Sources Sci. Technol.* **12** 39
[42] Silva P, Soto L, Kies W and Moreno J 2004 *Plasma Sources Sci. Technol.* **13** 329
[43] Hassan S, Clark E, Petridis C, Androulakis G, Chatzakis J, Lee P, Papadogiannis N and Tatarakis M 2011 *IEEE Trans. Plasma Sci.* **39** 2432
[44] Hassan S *et al* 2006 *Plasma Sources Sci. Technol.* **15** 614
[45] Bernard A *et al* 1998 *J. Mosc. Phys. Soc.* **8** 93
[46] Gribkov V, Bienkowska B, Borowiecki M, Dubrovsky A, Ivanova-Stanik I, Karpinski L, Miklaszewski R, Paduch M, Scholz M and Tomaszewski K 2007 *J. Phys. D: Appl. Phys.* **40** 1977